PERGAMON

International Journal of Heat and Mass Transfer 41 (1998) 2725–2733

International Journal of HEAT and MASS TRANSFER

Mass transfer rate study in rotating shallow electrochemical cells

F.-B. Weng, Y. Kamotani*, S. Ostrach

Department of Mechanical and Aerospace Engineering, Case Western Reserve University, Cleveland, OH 44106, U.S.A.

Received 12 June 1997; in final form 3 December 1997

Abstract

A scaling analysis and an experimental study of mass transfer rate in rotating shallow electrochemical cells are performed. The scaling analysis finds two convection regimes and shows that the parameters Ek and $Sc\,Ro_S$ are important to determine the mass transfer rate. The parameter $Sc\,Ro_S$ determines the thickness ratio of the viscous layer to the solutal layer as well as the convection regimes. The experimental study on mass transfer rate in rotating cells is conducted by utilizing the limiting current measurements with a cupric sulfate–sulfuric acid system. The overall mass transfer rates measured in the experiment are shown to agree with the scaling analysis and existing heat transfer data.

Nomenclature

Ac ratio of centrifugal to gravitational acceleration, $\Omega^2 R/g$

Ar aspect ratio, H/R

$\bar{C}, C$ dimensional and dimensionless Cu^{++} ion concentrations

$\bar{C}_b$ Cu^{++} ion bulk concentration

D mass diffusion coefficient

Ek Ekman number, $\nu/\Omega H^2$

F Faraday's constant

g gravitational acceleration

h_m total mass transfer coefficient

H thickness of test cell

i current density

n charge number

$\bar{p}, p$ dimensional and dimensionless pressures

$\bar{r}, r$ dimensional and dimensionless radial coordinates

R radius of test cell

$Ra_{\Omega R}$ centrifugal Rayleigh number, $\Omega^2\beta\Delta C R^4/\nu D$

Ro_S solutal Rossby number, $\beta\Delta C$

Sc Schmidt number, ν/D

$\overline{Sh}_H$ average Sherwood number based on thickness, $h_m H/D$

$\overline{Sh}_R$ average Sherwood number based on radius, $h_m R/D$

$\bar{u}, u$ dimensional and dimensionless r-component velocities

U radial reference velocity

$\bar{v}, v$ dimensional and dimensionless θ-component velocities

V azimuthal reference velocity

Ve reference overpotential

$\bar{w}$ dimensional z-component velocity

$\bar{z}, z$ dimensional and dimensionless vertical coordinates.

Greek symbols

β volumetric expansion coefficient due to concentration change

δ reference boundary layer thickness

δ_V Ekman layer thickness

δ_S solutal layer thickness

ΔC Cu^{++} ion concentration difference between two electrodes

$\bar{\theta}, \theta$ dimensional and dimensionless azimuthal coordinates

ν kinematic viscosity

ρ density

Ω rotation speed.

* Corresponding author. Tel.: 001 216 368 6455; fax: 001 216 368 6445.

0017-9310/98 $19.00
PII: S0017-9310(98)00015-5

1. Introduction

The present research was motivated by the discovery of a rotating nickel–zinc (Ni/Zn) battery system [1]. The rotating Ni/Zn battery provides very high energy density, power density, long cycle-life and no-toxicity at a comparatively low cost. The development and commercialization of a Ni/Zn battery system has been hindered for decades mainly due to the limited cycle-life of the Zn electrode during multiple recharging procedures [2]. The problem has been traced to: (i) formation and propagation of zinc dendrites which lead to cell shorting [3], and (ii) redistribution of zinc active material on the electrode (shape change), which causes gradual capacity loss [4].

By rotating the battery, which consists of a stack of flat cylinder cells, at a few hundred rpm, the Ni/Zn battery performance and cycle-life can be improved dramatically [5, 6]. The following effects have been noticed: (i) at rotations corresponding to 50 g (g is Earth's gravitational acceleration) the dendrite growth is nearly eliminated, the zinc electrode material redistribution is stabilized resulting in prolonged battery life to 1000 cycles, (ii) the charging electrical current density (electrode efficiency, A m^{-2}) is increased five times over the current density of a non-rotating battery. The successful control of dendrite growth and shape change on the zinc electrode has been attributed to the well-behaved solutal convection in the rotating battery. If these mechanisms are well understood, the most efficient means of preventing shape change and dendrite growth could be developed.

The single rotating cell in the Ni/Zn battery can be considered a rotating electrolyte solution (an excess KOH electrolyte solution containing zincate) inside a shallow cylinder subjected to an axial concentration difference. The mass transport process in the rotating fluid is complex. With superimposed rotating motion in the charging electrochemical cells, solutal buoyancy induces a swirling secondary flow through the coupling of centrifugal, Coriolis, gravitational acceleration and variation of density in the electrolyte solution.

The study of mass transport in a shallow rotating cell has not been reported in literature. Ostrach [7], however, showed that the mass convection and heat convection due to buoyancy flow in an enclosure can be analogous. Therefore, existing work on heat transfer in rotating shallow cylinders heated from above is reviewed. Ostrach and Braun [8] studied the cooling of a rotating space vehicle re-entering the atmosphere. It was concluded that the convection is very small, and the Coriolis force suppresses centrifugal buoyancy, inhibiting the heat transfer rate. The theoretical studies of this problem were continued by Barcilon and Pedlosky [9], and Homsy and Hudson [10]. Furthermore, the heat transfer rate of this configuration was investigated by experiments [11, 12] as well as numerical simulations [13, 14]. Those studies of heat transfer rate, however, did not cover the parametric ranges for rotating battery applications.

In the present work, solutal convection in shallow vertical rotating electrochemical cells subjected to concentration differences at two electrodes is studied. The main purpose of this study is to find the dependency of mass transfer rate on group parameters. The correlation of mass transfer rate will help to design rotating Ni/Zn battery optimally. The results from this study will be discussed in terms of dendrite formation and shape change on the electrode and how these processes can be prevented and controlled by the rotation of the battery.

As scaling analysis for the boundary layer regime is performed to determine the flow and solutal boundary layer characteristics. The proper dimensionless parameters are derived. The analysis also provides physical insight into the nature of the interaction among centrifugal, Coriolis forces and mass transport process in rotating battery. The experiment studies the mass transfer rate in the rotating electrochemical systems by utilizing the limiting current method [15].

2. Scaling analysis

Consider a flow in a shallow rotating cell with imposed concentration differences, as sketched in Fig. 1. In this analysis, the flow is assumed to be laminar, incompressible, axisymmetric, and steady. The analysis is limited to the boundary layer regions along the horizontal surfaces of a flat rotating cylinder. The following nondimensional parameters are introduced:

$$r=\frac{\bar{r}}{R},\quad z=\frac{\bar{z}}{\delta},\quad u=\frac{\bar{u}}{U},\quad v=\frac{\bar{v}}{V},$$

$$w=\frac{\bar{w}}{U\delta/R},\quad p=\frac{\bar{p}}{\rho U^2},\quad C=\frac{\bar{C}-\bar{C}_h}{\Delta C} \tag{1}$$

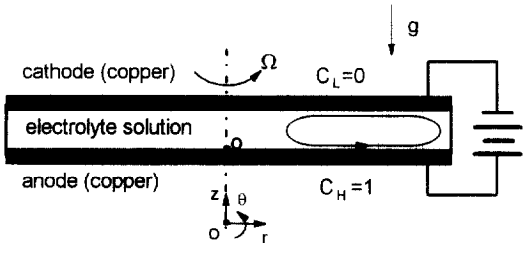

reaction at electrodes:
cathode: $Cu^{++} + 2e^- \rightarrow Cu$

anode : $Cu \rightarrow Cu^{++} + 2e^-$

electrolyte solution:
$CuSO_4 - H_2SO_4 - H_2O$

Fig. 1. Schematics of a rotating electrochemical cell.

where δ is either the velocity (δ_V) or the solutal (δ_S) boundary layer thickness. Then the dimensionless continuity, momentum and mass transfer equations for the boundary-layer region in rotating (with angular speed Ω) cylindrical coordinates are (Weng [16]):

$$\frac{1}{r}\frac{\partial}{\partial r}(ru)+\frac{\partial w}{\partial z}=0 \tag{2}$$

$$u\frac{\partial u}{\partial r}+w\frac{\partial u}{\partial z}-\frac{V^2}{U^2}\frac{v^2}{r}=-\frac{\partial p}{\partial r}+2\frac{VR\Omega}{U^2}v + \beta\Delta C\left(\frac{\Omega R}{U}\right)^2 Cr+\frac{\nu R}{U\delta^2}\frac{\partial^2 u}{\partial z^2} \tag{3}$$

$$u\frac{\partial v}{\partial r}+w\frac{\partial v}{\partial z}+\frac{uv}{r}=-2\frac{\Omega R}{V}u+\frac{\nu R}{U\delta^2}\frac{\partial^2 v}{\partial z^2} \tag{4}$$

$$u\frac{\partial C}{\partial r}+w\frac{\partial C}{\partial z}=\frac{1}{Sc}\frac{\nu R}{U\delta^2}\frac{\partial^2 C}{\partial z^2} \tag{5}$$

where the dimensionless pressure p in equation (3) is the modified pressure defined as

$$p=(\bar{p}+\rho g z-\rho\Omega^2 r^2/2)/(\rho U^2).$$

It should be noted that the centrifugal buoyancy force in equation (3) (the third term on the right) acts only within the solutal boundary layer and the viscous forces act within the velocity boundary layer. Therefore, two cases, in which the velocity boundary layer (δ_V) is either smaller or larger than the solutal boundary layer (δ_S), are discussed.

2.1. Case A: Velocity boundary layer thicker than solutal boundary layer

2.1.1. Region I ($\bar{z}<\delta_S$). Within the solutal boundary layer, the centrifugal buoyancy force is balanced by the viscous force in the radial momentum equation, equation (3). In addition, the convection and diffusion terms are balanced in the concentration equation, equation (5). Those two balances give

$$U\sim\Omega R\left(\frac{\beta\Delta C}{Sc}\right)^{1/2} \quad \text{and} \quad \delta_S\sim\left(\frac{\nu}{\Omega}\right)^{1/2}(Sc\,\beta\Delta C)^{-1/4}. \tag{6}$$

By balancing the Coriolis [the first right-hand side term of equation (4)] and viscous terms in the θ momentum equation and using equation (6) obtains

$$V\sim U\frac{\Omega\delta_S^2}{\nu}\sim\frac{\Omega R}{Sc}. \tag{7}$$

The Sherwood number for the whole cylinder can be obtained as

$$\overline{Sh}_H=\frac{h_m H}{D}=\frac{H}{\delta_S}\sim Ek^{-1/2}(Sc\,Ro_S)^{1/4} \tag{8}$$

or

$$\overline{Sh}_R=\frac{h_m R}{D}=\frac{R}{\delta_S}\sim(Ra_{\Omega R})^{1/4}.$$

2.1.2. Region II ($\delta_S<\bar{z}<\delta_V$)

Outside the solutal boundary layer, the above radial velocity $U\sim\Omega R(\beta\Delta C/Sc)^{1/2}$ continues to exist within the velocity boundary layer. By balancing the Coriolis and viscous forces in the momentum equations in the r and θ directions one obtains

$$U\sim V\sim\Omega R\left(\frac{\beta\Delta C}{Sc}\right)^{1/2} \quad \text{and} \quad \delta_V\sim\left(\frac{\nu}{\Omega}\right)^{1/2}. \tag{9}$$

The velocity boundary layer is called the Ekman layer. Since the analysis is valid when the Ekman layer exists inside the cell, the condition of $H/\delta_V\sim Ek^{-1/2}>1$ must be satisfied in this case. Also, the ratio of two boundary layer thicknesses is $\delta_V/\delta_S\sim(Sc\,Ro_S)^{1/4}$, so the initial assumption of $\delta_V\gg\delta_S$ is satisfied only when $(Sc\,Ro_S)^{1/4}\gg 1$. Within the Ekman layer the ratio of inertia to viscous forces ($U\delta_V^2/\nu R$) is given by $(\beta\Delta C/Sc)^{1/2}$, which is much less than unity, so the inertia forces do not appear in the above analysis.

The above scaling laws are tabulated in Table 1. The flow field near the bottom wall for this case is sketched in Fig. 2. In the present experimental configuration, the velocity component u is radially outward along the bottom wall and radially inward along the top wall. Then, the azimuthal velocity component v, which is induced by the Coriolis force, is against the cylinder rotation direction (negative sign) near the bottom wall and in the direction of rotation (positive) near the top wall. The magnitude of azimuthal velocity decreases outside the boundary layer (δ_V) as the Coriolis force diminishes, and changes its sign at a certain location. The Coriolis force induced by v in equation (3) is negative (positive) when u is positive (negative), which means that the radial flow tends to be retarded by the Coriolis force. Since the centrifugal buoyancy force acts mainly in the region δ_S, the radial velocity has a peak near the edge of δ_S and its magnitude decreases away from that location due both to viscous retardation and to the Coriolis force mentioned above. Along the bottom wall the total mass flux in the velocity boundary layer increases in the flow direction as the radial velocity increases with increasing radius. Consequently, an axial fluid motion is induced toward the wall by entrainment. The opposite is true along the top wall, so the axial flow is from the top to bottom walls.

2.2. Case B: Velocity boundary layer thinner than solutal boundary layer

2.2.1. Region I ($\bar{z}<\delta_V$). Within the velocity boundary layer, the centrifugal buoyancy is balanced by the viscous force in the radial momentum equation. The Coriolis and viscous forces are balanced in the momentum equations

Table 1
Scaling laws in boundary layer regions along horizontal surfaces of a flat rotating cylinder

		Case A $\delta_V \gg \delta_S$ $(Sc\,Ro_S \gg 1)$	Case B $\delta_V \ll \delta_S$ $(Sc\,Ro_S \ll 1)$
Solutal boundary layer thickness, δ_S		$(\nu/\Omega)^{1/2}(Sc\,Ro_S)^{-1/4}$	$(\nu/\Omega)^{1/2}(Sc\,Ro_S)^{-1}$
Ekman boundary layer thickness, δ_V		$(\nu/\Omega)^{1/2}$	$(\nu/\Omega)^{1/2}$
Velocity U	Region I	$\Omega R(Ro_S/Sc)^{1/2}$	$\Omega R\,Ro_S$
	Region II	$\Omega R(Ro_S/Sc)^{1/2}$	$\Omega R\,Sc^2(Ro_S)^3$
Velocity V	Region I	$\Omega R/Sc$	$\Omega R\,Ro_S$
	Region II	$\Omega R(Ro_S/Sc)^{1/2}$	$\Omega R\,Ro_S$
Sherwood number: H/δ_S, or R/δ_S		$Ek^{-1/2}(Sc\,Ro_S)^{1/4}$ or $(Ra_{\Omega R})^{1/4}$	$Ek^{-1/2}(Sc\,Ro_S)$
Ratio of two boundary layer, δ_V/δ_S		$(Sc\,Ro_S)^{1/4} \gg 1$	$(Sc\,Ro_S)^{1} \ll 1$

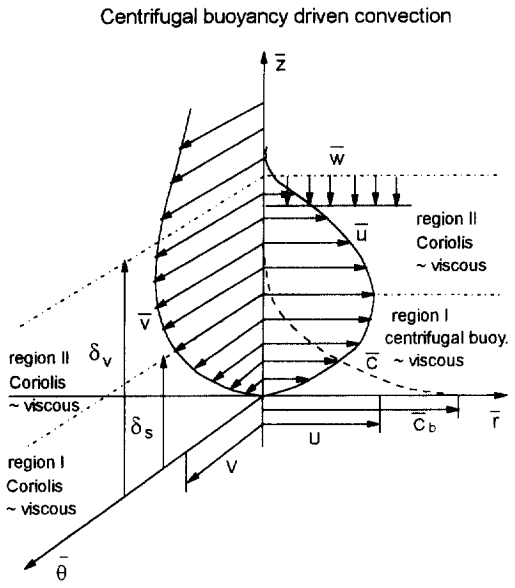

Fig. 2. Boundary layer structure for Case A ($\delta_S \ll \delta_V$).

in the r and θ directions (the inertia forces are relatively small as in Case A). Under those conditions, one obtains

$$U \sim V \sim \Omega R\beta\Delta C \quad \text{and} \quad \delta_V \sim (\nu/\Omega)^{1/2}. \tag{10}$$

For later use, the axial entrainment flow velocity toward δ_V can be estimated as $U\delta_V/R \sim (\Omega\nu)^{1/2}\beta\Delta C$.

2.2.2. Region II ($\delta_V < \bar{z} < \delta_S$)

Outside the velocity boundary layer, but within the solutal layer, the viscous effect is less important. Therefore, in the r-momentum equation the Coriolis force is balanced by the centrifugal buoyancy, which gives

$$V \sim \Omega R\beta\Delta C. \tag{11}$$

In the θ-momentum equation, the Coriolis term can be balanced only by the viscous term, from which one obtains,

$$\frac{U}{V} \sim \frac{\nu}{\Omega\delta_S^2}. \tag{12}$$

But since the effect of viscosity is weak in this region, the ratio U/V must be much less than unity.

The diffusion growth of solutal boundary layer is counteracted by the convection toward the wall. Then, by balancing the axial convection and diffusion terms in equation (5) with the axial velocity given by the aforementioned entrainment velocity, one obtains

$$\delta_S \sim \left(\frac{\nu}{\Omega}\right)^{1/2}(Sc\,\beta\Delta C)^{-1} = \left(\frac{\nu}{\Omega}\right)^{1/2}(Sc\,Ro_S)^{-1}. \tag{13}$$

Then, the Sherwood number is given as

$$\overline{Sh}_H \sim H/\delta_S \sim Ek^{-1/2}(Sc\,Ro_S). \tag{14}$$

Since the initial assumption is that the solutal boundary layer exists, namely, $H/\delta_S > 1$, therefore, $Sc\,Ro_S > Ek^{1/2}$ for this analysis to be valid. Also, if the initial assumption of $\delta_S \gg \delta_V$ is to be satisfied, it is required that $\delta_V/\delta_S \sim Sc\,Ro_S \ll 1$. Then, from equation (12) one obtains $U/V \sim (Sc\,Ro_S)^2$, which is much less than unity.

The above results are tabulated in Table 1 and the flow field near the bottom wall is illustrated in Fig. 3. The radial velocity outside δ_V is suppressed by the Coriolis force. Therefore, in both Cases A and B (Figs. 2 and 3) the radial velocity is relatively small outside the velocity boundary layer. As a result, the azimuthal velocity dominates in the core region, namely the region between the top and bottom boundary layers.

One important difference between Cases A and B is that in Case A the solutal boundary layer development, and thus the mass transfer rate, is controlled by the centrifugal buoyancy, while in Case B it is controlled by the Ekman layer flow and the associated axial flow. In that sense, the convection in Case A is analogous to natural convection in a rectangular container without rotation, so it may be useful to compare those two cases. Table 2 shows comparisons of scaling laws between centrifugal convection and natural convection. The velocity scale,

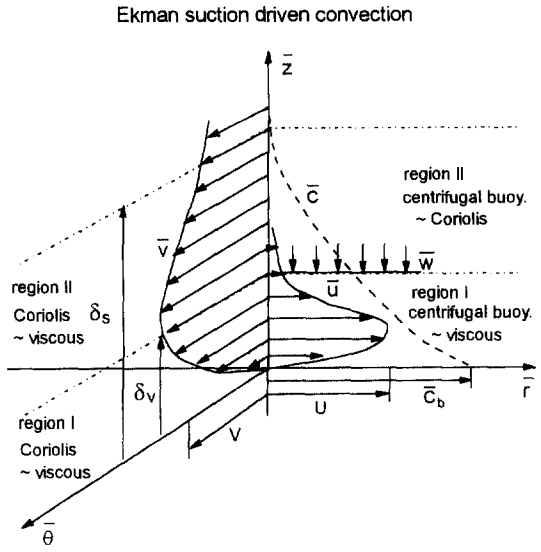

Fig. 3. Boundary layer structure for Case B ($\delta_V \ll \delta_S$).

solutal layer thickness, and mass transfer rate are the same as long as $Ra_{\Omega R}$ is used for the centrifugal convection. The viscous layer thickness is different between these two cases: the viscous layer thickness in the centrifugal convection (Ekman layer) is uniform in the radial direction and is of the order $(\nu/\Omega)^{1/2}$, which is independent of ΔC and Sc. In contrast, the natural convection viscous layer is of the order $(LRa_L^{-1/4}\, Sc^{1/2})$ for $Sc \gg 1$, which depends on ΔC, Sc and length scale. The ratio δ_V/δ_S scales with $(Sc\, Ro_S)^{1/4}$ in the centrifugal convection and with $Sc^{1/2}$ in the natural convection. Then, for a given fluid and ratio δ_V/δ_S is constant in the natural convection but it depends on Ro_S or $\beta\Delta C$ in the centrifugal convection. As discussed above, the radial flow in the core region tends to be suppressed by the Coriolis force in the centrifugal convection. As a result, the fluid in the core tends to be stably stratified (increasing density toward the outer edge).

The above scaling analysis shows that the mass transfer rate in the rotating cells is governed by $Ek^{-1/2}$ and $Sc\, Ro_S$ or $(Sc\, Ro_S)^{1/4}$, depending on the convection regime. Also, the $Sc\, Ro_S$ number is the most important parameter to determine the two convection regimes. In battery applications, we generally have $Ek \ll 1$ and $Sc\, Ro_S \gg 1$ so that the rotating electrochemical cell has a large inviscid core, and the mass transfer rate is primarily controlled by centrifugal buoyancy. Also, the results of scaling analysis can be applied to the early heat transfer studies in rotating cylinders. The theoretical studies of this problem include Ostrach and Braun [8], Barcilon and Pedlosky [9], and Homsy and Hudson [10]. Air is considered as the rotating fluid in those analyses, so that Pr is order one and $Pr\,\beta\Delta T$ is much smaller than unity. Moreover, those analytical studies are limited to parametric ranges of $Pr\,\beta\Delta T \leqslant Ek^{1/2}$. Therefore, unlike in the present problem, no thermal boundary layer exists in those analyses. The experiment data in [11, 12] show two convection regimes in rotating cylinders. In those studies, $Gr_\Omega^{1/4}$ (or $Ek^{-1/2}(\beta\Delta T)^{1/4}$) and $Ek^{-1/2}\, Pr\,\beta\Delta T$ are used as the characteristic parameters to correlate the two convection regimes, which is in good agreement with the present scaling law. In one convection regime, the parametric ranges are $Ek \sim O(1)$ and $Pr\,\beta\Delta T \gg 1$ to minimize the Coriolis force in the whole cylinder, so that centrifugal buoyancy dominates in the whole test section. The other flow regime has parametric ranges of $Ek \ll 1$ and $Pr\,\beta\Delta T \ll 1$ to maximize the Coriolis force effect.

3. Experimental method

A schematic diagram of the experimental facility and the test section are illustrated in Fig. 4. The rotating system consists of two major units, a rotary and a station-

Table 2
Comparisons of scaling laws between centrifugal buoyancy convection and natural convection

		Centrifugal buoyancy convection in rotating cylinder	Natural convection in rectangular enclosure
Case of		$\delta_V \gg \delta_S$ $(Sc\, Ro_S \gg 1)$	$\delta_V \gg \delta_S$ $(Sc \gg 1)$
Solutal boundary layer thickness, δ_S		$(\nu/\Omega)^{1/2}(Sc\, Ro_S)^{-1/4}$	$L\, Ra_L^{-1/4}$
Viscous layer thickness, δ_V		$(\nu/\Omega)^{1/2}$	$L\, Ra_L^{-1/4}\, Sc^{1/2}$
Velocity U	Region I	$\Omega R(Ro_S/Sc)^{1/2}$	
	Region II	$\Omega R(Ro_S/Sc)^{1/2}$	$(D/L)Ra_L^{1/2}$
Velocity V	Region I	$\Omega R/Sc$	
	Region II	$\Omega R(Ro_S/Sc)^{1/2}$	
Sherwood number H/δ_S, or R/δ_S		$Ek^{-1/2}(Sc\, Ro_S)^{1/4}$ or $Ra_{\Omega R}^{1/4}$	$Ra_L^{1/4}$
Ratio of two boundary layers, δ_V/δ_S		$(Sc\, Ro_S)^{1/4} \gg 1$	$Sc^{1/2} \gg 1$

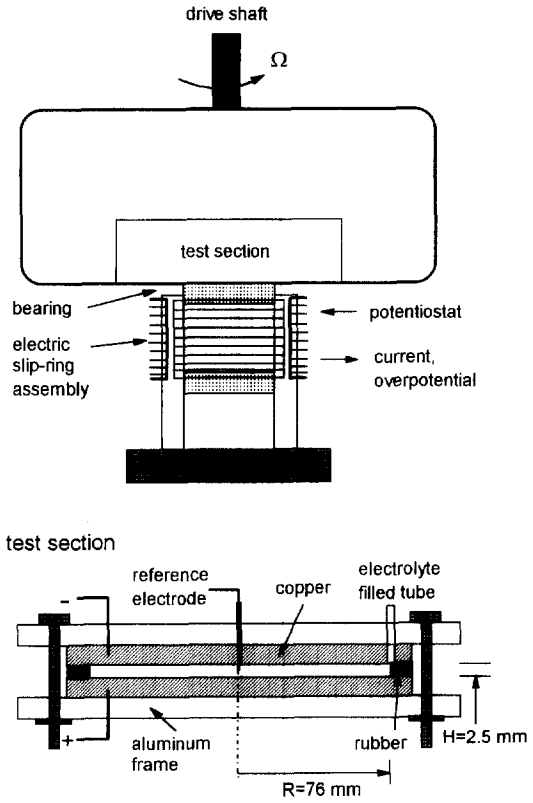

Fig. 4. Schematics of experimental apparatus and test section.

ary frame. The rotary frame is made of two square, parallel plates and is held together by eight vertical bars. The frame is connected to the upper unit by a drive shaft and an aluminum flange. A milling machine is used to rotate the frame. The weight of the milling machine provides the stability of the experimental facility. The assembled test section is attached to the bottom of a rotary frame and is connected to the accessory wires. The stationary frame consists of a supporting lower platform, two radial thrust bearings, and an electric slip-ring assembly. In order to supply electric power to the electrodes and record the output currents and voltages, the slip-ring assembly connects the test section with a potentiostat power supply and a digital multimeter.

The test section is designed and constructed to simulate the mass transport in a rotating shallow, cylindrical electrochemical cell by utilizing the cupric sulfate–sulfuric acid system. The test section consists of two horizontal electrode disks, which serve as the cathode and anode, and a vertical annular spacer which separates the two electrodes and acts as an insulating boundary for the mass transfer. The electrodes are constructed of 6.6 mm thick copper plate with 179 mm width and 75 mm side length. Two lead wires are attached to the electrodes to provide the potential difference between the electrodes. An insulated copper wire (0.84 mm diameter) serves as the reference electrode to keep the constant potential reference to the working electrode. It is positioned at the center of the top electrode. An opening on the side of the test section is used to fill the system with electrolyte solution. This opening also allows air bubbles to escape from the test section during filling. The rubber spacer is 2.5 mm thick and 76 mm inside radius. The outside shape is hexagonal, same as that of the electrode. The test section is then attached to two high strength aluminum square plates by four sets of long screws located at corners. This design of the test section allows its safe operation during high speed rotation. The Model 173 Potentiostat/Galvanostat, manufactured by Princeton Applied Research Co., offers complete flexibility in potential or current control for electrochemical experiments. A Model 178 Electrometer Probe is connected to the reference electrode.

A cupric sulfate–sulfuric acid solution ($CuSo_4$–H_2SO_4–H_2O) is chosen to simulate zincate–alkaline solution used in Ni/Zn batteries. The advantages of cupric sulfate–sulfuric acid solution include slow roughness growth, well-known electrochemical reaction, and similar fluid properties to zincate–alkaline solution (Liu et al. [17]).

To minimize the error of initial surface condition, the surface of the electrode must be carefully polished. The polishing process starts with an emery paper no. 200, and progressing sequentially down to no. 600. The working surface of the electrode is then washed with tap water followed by distilled water. Technical grade methanol is applied in a final step to dry the surface and to increase the wetting action of the electrolyte solution.

The mass transfer rate is determined based on the measurement of limiting current in the present experiments. The limiting current method for measuring the mass transfer rate in electrochemical systems has been addressed in detail by Selman and Tobias [15]. To determine the limiting current the potential difference between the working electrode and reference probe is increased stepwise, starting from zero, and the current is monitored. At each potential setting, the current quickly approaches a quasi-steady state (2–3 min). The experiment is terminated immediately following establishment of the limiting current plateau to avoid excessive hydrogen evolution. The mass transfer coefficient can be defined in the usual manner, $h_m = i/nF\Delta C$. After the data are recorded, the test section is opened to examine the deposition pattern.

The dimensions of test section in this experiment are: radius $R = 76$ mm and height $H = 2.5$ mm. The physical properties of the electrolyte solution are: mass diffusion coefficient $D = 4.86 \times 10^{-10}$ m^2 s^{-1} at 25°C, kinematic viscosity $\nu = 1.16 \times 10^{-6}$ m^2 s^{-1} at 25°C, volumetric expansion coefficient $\beta = 0.112$/M, concentration difference between electrodes $\Delta C = 0.02\,\text{M} \sim 0.16\,\text{M}$, rotation speed of test section $\Omega = 150$–400 rpm (15.7–41.9 rad/s).

The corresponding ranges of dimensionless parameters are: $Ek = 4.3\times10^{-3}$–1.15×10^{-2}, $Ro_S = 2.2\times10^{-3}$–1.8×10^{-1}, $Ac = 1.92$–13.6, $Ar = 0.033$, $Sc = 2380$ and $Ra_{\Omega R} = 3.3\times10^{10}$–$9.4\times10^{11}$. The average Sherwood number is defined as $\overline{Sh}_H = h_m H/D$ or $\overline{Sh}_R = h_m R/D$. The estimated errors for the dimensionless parameters are: $Sc\,Ro_S$ is within 10%, Ek 4%, Ac 2%, $Ra_{\Omega R}$ 11%, h_m 5%, and $\overline{Sh}_H$, $\overline{Sh}_R$ are within approximately 12 and 11%, respectively.

4. Experimental results and discussion

Figure 5 shows the relations between current density and overpotential at rotating speeds between 150 and 400 rpm for a 0.08 M concentration difference. As seen in the figure, the current is independent of the rotation rate when the overpotential is below 200 mV. This is because the current is controlled by the electrochemical reaction and overpotential, since the convection is still very weak and the fluid is nearly in solid body rotation. The figure also shows that the limiting current density is increased with increasing rotation rate. This is due to the fact that larger centrifugal body forces increase the convection and enhance the mass transfer rate. As seen in Fig. 5, the overpotential to obtain the limiting current also increases with increasing rotation rate for the following reason. As will be discussed later, the mass transfer becomes more non-uniform over the electrode surface in higher rotation speed. Therefore, not all the local electrode surface reaches the limiting current at the same overpotential, so that the overpotential to obtain the limiting current over the entire electrode surface becomes larger than the value we would obtain if the mass transfer is uniform. Eventually the overpotential becomes sufficiently large that hydrogen generation occurs near the limiting current condition. As a result, there is a certain degree of ambiguity as to determining the limiting current value for high rotation rates. Generally, the slope and curvature of the current-overpotential curve decrease with increasing potential up to a certain current and then starts to increase due to gas generation. In the present work the limiting current is considered to lie in the region where the curvature of the current-overpotential curve is reduced to a relatively small value but below the current at which the slope starts to increase due to hydrogen generation. For example, Fig. 5 indicates the limiting current value so determined for the 400 rpm curve, together with a range of uncertainty. The uncertainty is about $\pm10\%$ for that case. The uncertainty is smaller in other tests.

The values of limiting current density, which is proportional to the total mass transfer rate, measured under various conditions are presented in Fig. 6. For a given ΔC the mass transfer rate increases generally with increasing rotation speed for the reason discussed above. The figure also shows that as ΔC increases, the mass transfer rate increases and its dependence on the rotation rate becomes stronger.

The measured mass transfer rates are correlated according to the scaling laws obtained earlier. Figure 7 shows the average Sherwood number vs. the Ekman number for three different values of $Sc\,Ro_S$. Earlier, the scaling analysis shows that when $Ek \ll 1$ and $Sc\,Ro_S \gg 1$, the viscous Ekman layer is thin along the horizontal surface, which implies that the test section has a large inviscid core area. Also, the average solutal layer is thinner than the Ekman layer, hence the convection in the boundary layer is dominated by centrifugal buoyancy. The scaling analysis showed that the mass transfer rate scales as $\overline{Sh} \sim Ek^{-1/2}$. This expression is generally consistent with the present results as seen in Fig. 7. However, near $Sc\,Ro_S = 21$ and $Ek = 0.0043$ (largest $Sc\,Ro_S$ and smallest Ek in the present experiment) the trend of $\overline{Sh}_H$ appears to deviate from the scaling law. The reason for the deviation is explained below.

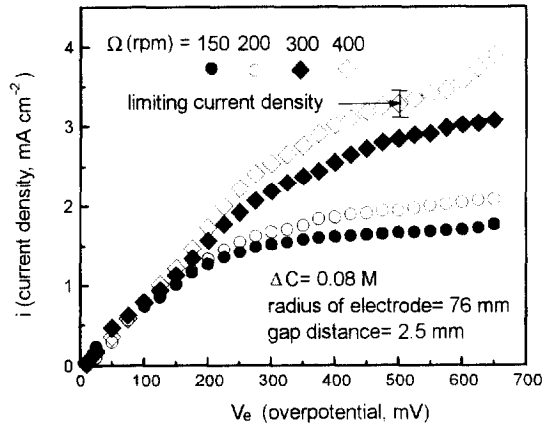

Fig. 5. Current density vs. overpotential in rotating cells for $\Omega = 150$–400 rpm and $\Delta C = 0.08$ M.

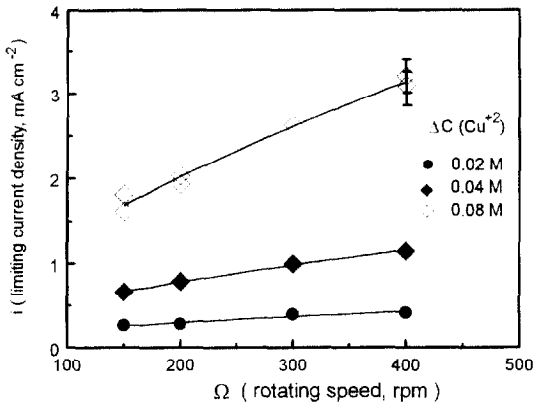

Fig. 6. Limiting current density vs. rotating speed for $\Delta C = 0.02$, 0.04 and 0.08 M.

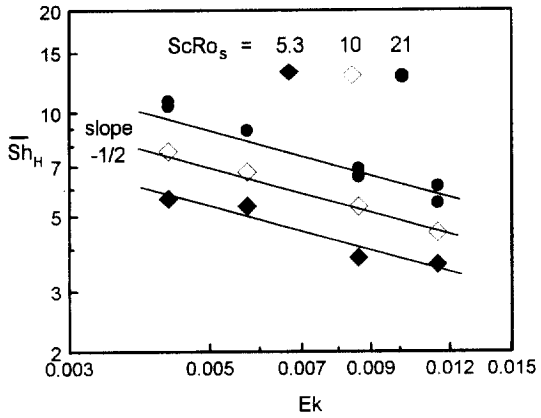

Fig. 7. Sherwood number vs. Ekman number for $Ar = 0.033$.

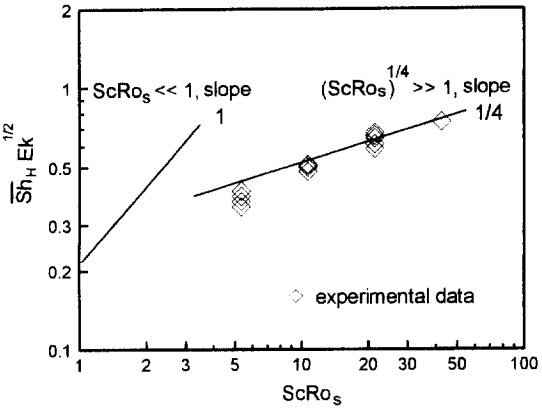

Fig. 8. $\overline{Sh}_H Ek^{1/2}$ vs. $Sc\,Ro_S$ number for $Ar = 0.033$.

A different phenomenon from other cases is observed when $Ek = 0.0043$ ($\Omega = 400$ rpm) and $Sc\,Ro_S = 21$ ($\Delta C = 0.08$ M) in the present experiment. The limiting current does not become steady and it fluctuates within about 5–10% of the average value. This situation is different from other cases where the current can reach a steady state and their variation is less than 2%. Also, these results are repeatable within the experimental error. The fact that the current becomes fluctuating beyond certain conditions suggests that there is a critical parameter to describe the onset of unsteady or turbulent condition in a rotating electrochemical cell. The unsteady or turbulence effect can enhance the mass transfer rate. The unsteady or turbulence mechanism in a rotating system is more complex than in the natural convection counterpart because both Ekman layers and Coriolis force are present in the centrifugal buoyancy convection. The unsteady state may be induced by the centrifugal convection or may come from the interaction between the Ekman layer and the inviscid core. A detailed experimental study is needed to clarify this. The present study focuses mainly on the laminar convection regime.

The mass transfer data are plotted as $\overline{Sh}_H Ek^{1/2}$ vs. $Sc\,Ro_S$ in Fig. 8. In the present experiment the value of $Sc\,Ro_S$ is larger than unity so that the situation is closer to Case A than Case B. However, since the value of $(Sc\,Ro_S)^{1/4}$ ranges from 1.5–2.6, which is near unity, the centrifugal convection regime is not expected to be very well established. The data for $Sc\,Ro_S = 21$, $Ek = 0.0043$ tend to scatter for the reason discussed above. Excluding those data with large current fluctuations, the data in Fig. 8 show the slope of the $\overline{Sh}_H Ek^{1/2}$–$Sc\,Ro_S$ curve is closed to 1/4 for large values of $(Sc\,Ro_S)^{1/4}$, as predicted by the scaling analysis. The data for $Sc\,Ro_S = 5.3$ deviate from the power law because the value of $(Sc\,Ro_S)^{1/4}$ is near unity (1.5). The results also indicate that the Coriolis force has a minor effect for inhibiting the mass transfer rate in the rotating electrochemical cells.

Figure 9 shows the Sherwood number vs. $Ra_{\Omega R}$ together with available experimental data taken in heat transfer experiments. Hudson et al. [11] published the heat transfer rate data in the figure for $Ra_{\Omega R}$ between 10^7 and 10^9. The present tests are in the range $3 \times 10^{10} < Ra_{\Omega R} < 1 \times 10^{12}$. Both data, together covering a wide range of $Ra_{\Omega R}$, are correlated by the 1/4-power law reasonably well.

Finally, some important implications of the present results to rotating battery applications are discussed. In the battery applications, since the range of Ek is small, there exists a large inviscid core. Coriolis force dominates the inviscid core, but this force has a minor effect on the

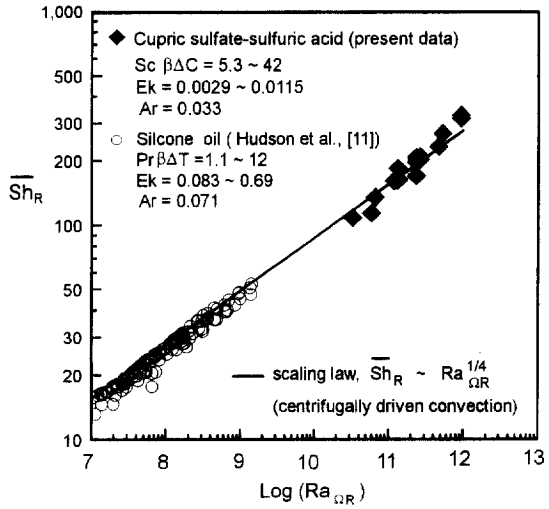

Fig. 9. Sherwood number vs. centrifugal Rayleigh number for present and published data.

mass transfer rate. The solutal layer is smaller than the Ekman layer, and the solutal layer, controlled by centrifugal buoyancy, determines the mass transfer rate in the rotating cells. The induced convection in the rotating Ni/Zn battery can inhibit the dendrite growth and stabilize the zinc material redistribution. Generally, the dendrites appear when the charging current is close to the limiting current [3]. When the battery rotates at high speed, the limiting current is increased several times over that of a stationary battery. Therefore, one can charge the battery efficiently at a charging current that is below the current for dendrite formation. This is the principal factor due to which the dendrites disappear in the rotating, charging Ni/Zn battery. Moreover, the convection may be used to control the shape change phenomenon. Although the mechanism of shape change is still unclear, the basic shape change phenomenon is that the zinc material depletes from the edge area to the center during the multiple recharge procedure [4]. This process degrades the battery capacity. In the present experiment the deposited surfaces of copper electrodes are observed for each experimental run. The rough-red deposition is seen near the edge of electrode and the smooth-pink deposition near the center area [16]. Such deposition pattern is caused by the fact that the high centrifugal field in the rotating cells causes more mass transfer in the edge area than near the center area. Therefore, the centrifugal convection may provide efficient means of compensating the mass transfer rate near the edge area of the zinc electrode thereby prolonging the battery cycle-life.

5. Conclusions

The mass transfer rate for rotating shallow electrochemical systems is studied in the present work. In addition to a scaling analysis, the overall mass transfer rates are measured experimentally by the limiting current method. In the scaling analysis, two convection mechanisms are delineated for the boundary layer regime of the flow in a rotating cell: one is centrifugal dominated convection and the other is called Ekman suction convection. The criterion for determining the type of convection is the thickness ratio of viscous layer to solutal layer, or the parameter $Sc\,Ro_S$. The mass transfer rates of both convection mechanisms are dependent on Ek and $Sc\,Ro_S$. The measured mass transfer rates are found to be in good agreement with the scaling analysis as well as the published data. Based on the experimental results the convection phenomena in rotating electrochemical systems are beneficial in controlling the dendrite formation and shape change. The mass transfer rate information obtained herein could be used to optimize the design of a high performance and long life rotating Ni/Zn battery.

Acknowledgement

This work was supported by NASA's Office of Life and Microgravity Science and Applications under Grant No. NAG3-886.

References

[1] Tamminen P. U.S. Patent No. 4 521 497 and 4 684 585, 1987.
[2] Mclarnon FR, Cairns EJ. The secondary alkaline zinc electrode. Journal of The Electrochemical Society 1991;138(2):645–64.
[3] Diggle JW, Despic AR, Bockris JO'M. The mechanism of the dendritic electrocrystallization of zinc. Journal of The Electrochemical Society 1969;116(11):1503–14.
[4] Einerhand REF, Visscher W, de Goeij JJM, Barendrecht E. Zinc electrode shape change II. Process and mechanism. Journal of The Electrochemical Society 1991;138(1):7–17.
[5] Tamminen P, Salkind AJ. High power density, long life, bipolar nickel–zinc batteries, power sources 12-Proc. International Power Sources Conference 16. Brighton, England, 1988.
[6] Salkind AJ, Kantner E, Grun C. Diffusion limitations to cycle life of nickel–zinc batteries and effects of vibration and rotation. In: Salkind et al., editors. Proceedings of the Symposium on Rechargeable Zinc Batteries 1995;95(14): 160–81.
[7] Ostrach S. Natural convection in enclosures. Journal of Heat Transfer 1988;110:1175–90.
[8] Ostrach S, Braun WH. Natural convection inside a flat rotating container. NACA Technical Note 4323, 1958.
[9] Barcilon V, Pedlosky, J. On the steady motions produced by a stable stratification in a rapidly rotating fluid. Journal of Fluid Mechanics 1967;29(4):673–90.
[10] Homsy GM, Hudson JL. Centrifugally driven thermal convection in a rotating cylinder. Journal of Fluid Mechanics 1969;35(1):33–52.
[11] Hudson JL, Tang D, Abell S. Experiments on centrifugally driven thermal convection in a rotating cylinder. Journal of Fluid Mechanics 1978;86(1):147–59.
[12] Abell S. Thermal convection in rotating fluids. Ph.D. thesis, University of Illinois at Urban-Champaign, 1974.
[13] Chew JW. Computation of convective laminar flow in rotating cavities. Journal of Fluid Mechanics 1985;153:339–60.
[14] Gou Z-Y, Zhang C-M. Thermal drive in centrifugal fields—mixed convection in a vertical rotating cylinder. International Journal of Heat and Mass Transfer 1992;35(7):1635–44.
[15] Selman JR, Tobias CW. Mass transfer measurements by the limiting-current technique. In: Drew et al., editors. Advances in Chemical Engineering. New York: Academic Press, 1978;10:211–319.
[16] Weng F-B. Mass transport process in rotating shallow electrochemical cells. Ph.D. thesis, Cleveland, Ohio: Case Western Reserve University, January, 1997.
[17] Liu MB, Cook GM, Yao NP. Vibrating zinc electrodes in Ni/Zn batteries. Journal of the Electrochemical Society 1982;129(5):913–20.